Humic Acid with Vertical Adsorption Conformation Enhanced the Transport of Petroleum Hydrocarbon-Contaminated Colloids

Environmental Science and Technology

Ma, Jie; Zhou, Ping; Liu, Yong; Lian, Wanli; Feng, Bingcong et al

https://doi.org/10.1021/acs.est.4c11233

This publication is made publicly available in the institutional repository of Wageningen University and Research, under the terms of article 25fa of the Dutch Copyright Act, also known as the Amendment Taverne.

Article 25fa states that the author of a short scientific work funded either wholly or partially by Dutch public funds is entitled to make that work publicly available for no consideration following a reasonable period of time after the work was first published, provided that clear reference is made to the source of the first publication of the work.

This publication is distributed using the principles as determined in the Association of Universities in the Netherlands (VSNU) 'Article 25fa implementation' project. According to these principles research outputs of researchers employed by Dutch Universities that comply with the legal requirements of Article 25fa of the Dutch Copyright Act are distributed online and free of cost or other barriers in institutional repositories. Research outputs are distributed six months after their first online publication in the original published version and with proper attribution to the source of the original publication.

You are permitted to download and use the publication for personal purposes. All rights remain with the author(s) and / or copyright owner(s) of this work. Any use of the publication or parts of it other than authorised under article 25fa of the Dutch Copyright act is prohibited. Wageningen University & Research and the author(s) of this publication shall not be held responsible or liable for any damages resulting from your (re)use of this publication.

For questions regarding the public availability of this publication please contact openaccess.library@wur.nl

Environmental Science & Technology

pubs.acs.org/est

Article

Humic Acid with Vertical Adsorption Conformation Enhanced the Transport of Petroleum Hydrocarbon-Contaminated Colloids

Jie Ma,* Ping Zhou, Yong Liu, Wanli Lian, Bingcong Feng, Li Li, Yujie Zhao, Liping Weng, Gangxing Lei, and Haiming Li*

Cite This: https://doi.org/10.1021/acs.est.4c11233

Read Online

ACCESS | Metrics & More | Article Recommendations | Supporting Information

Downloaded via WAGENINGEN UNIV & RESEARCH on February 14, 2025 at 07:02:17 (UTC).
See https://pubs.acs.org/sharingguidelines for options on how to legitimately share published articles.

ABSTRACT: Humic acid (HA) enhances colloidal transport in porous media, yet the mechanisms by which the HA adsorption conformation affects colloid transport remain unclear. This study investigated the influence of HA on the transport of petroleum-hydrocarbon-contaminated soil colloids (TPHs-SC) in saturated sand columns. The presence of TPHs on the colloidal surface occupied adsorption sites, hindering HA from forming a horizontal adsorption conformation, as observed on uncontaminated soil colloids (SC). Instead, a vertical adsorption conformation was formed, reducing the overall adsorption of HA. Vertically adsorbed HA increased the colloidal diffuse double-layer potential and extended the Derjaguin−Landau−Verwey−Overbeek energies between colloids and water-bearing media. This was evidenced by higher ζ potentials (−28.5 to −34.0 mV) and enhanced TPHs-SC transport compared to SC (ζ potentials ranging from −25.2 to −29.5 mV) in the presence of HA, particularly under alkaline conditions. Additionally, weak van der Waals and electrostatic interactions between TPHs near colloidal surfaces and free HA/TPHs formed a zonal distribution, facilitating the cotransport of colloids with TPHs. These findings underscore the significance of the HA adsorption conformation in TPHs-SC transport and provide insights into the critical mechanisms from an environmental structural chemistry perspective.

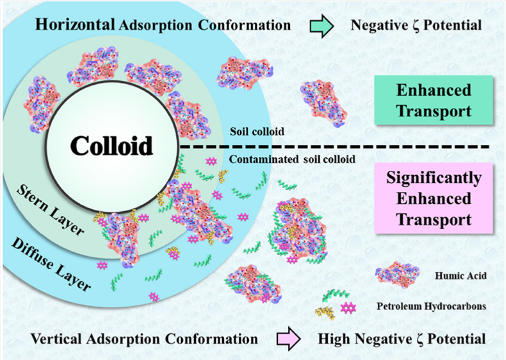

KEYWORDS: *humic acid, soil colloids, total petroleum hydrocarbons, transport, environmental structural chemistry*

■ INTRODUCTION

Petroleum extraction, storage, transportation, and petrochemical industrial processes contaminate soil and groundwater with petroleum hydrocarbons.[1] Total petroleum hydrocarbons (TPHs) comprise chemicals such as benzene, toluene, ethylbenzene, xylene, long-chain alkanes/alkenes, and polycyclic aromatic hydrocarbons,[2] which can cause cancer and birth defects, posing a direct threat to human health.[3,4] Remediation of TPH-contaminated soil is challenging, leading to long-lasting damage.[5]

Soil colloids (SC) are extremely fine soil particles, including clay minerals, metal oxides, and organic macromolecules, with sizes ranging from 1 to 1000 nm. SC present in natural porous media can aid the movement of pollutants by adsorption.[6] While numerous studies have examined the transport of SC[7−9] and their cotransport with contaminants,[10−13] research on the transport of SC with TPHs is limited. Hydrophobic TPHs adsorb onto the SC, altering their surface properties and transportation. When SC-carrying TPHs transport through the vadose zone to aquifers, they pose a significant groundwater contamination risk. Although previous studies have reported experimental and theoretical developments on the cotransport of colloid-contaminant and colloid−colloid interaction,[14−20] the cotransport of soil organic matter, organic contaminants, and soil colloids has not been studied thoroughly.

The structure of organo-mineral associations in soils is described by the "zonal model", which suggests that soil organic matter (SOM) attaches to mineral surfaces in a specific sequence of contact, hydrophobic, and kinetic zones.[21,22] According to this model, the polar functional groups of organic compounds (including SOM and organic contaminants) interact with soil mineral hydroxyl groups via ligand exchange, exposing the hydrophilic portions of the molecule to the aqueous phase.[22] Additionally, other organic molecules may interact via weak intermolecular interactions with the hydrophilic portions of the hydrophobic zone, forming an outer region.[22] In TPH-contaminated soil, TPHs with complex compositions preferentially occupy the contact and hydrophobic zones, forming a hydrophobic layer[23] that alters SC transport.

Received: October 18, 2024
Revised: January 17, 2025
Accepted: January 21, 2025

ACS Publications

© XXXX American Chemical Society

Humic acid (HA) plays a crucial role in promoting colloids transport by imparting a negative charge to colloids.[24−28] HA readily attaches to the SC surface, significantly altering surface chemistry and retention-repulsion properties in pore media by introducing negative charges.[7] For TPH-contaminated SC (TPHs-SC), HA adsorption can modify the distribution of TPH molecules on the colloidal surface. However, the loading behavior of HA may vary under TPH interference due to site occupation and weak interactions between TPHs and HA. The adsorption configurations of TPHs and HA on colloids ultimately control their transport mechanisms.

Petroleum hydrocarbons, primarily composed of hydrogen and carbon derived from crude oil, may include compounds such as hexane, mineral oils, benzene, toluene, xylenes, naphthalene, and fluorene.[29−33] Due to the complexity of TPH composition, the adsorption configurations of TPHs and HA are inherently intricate. HA's capacity to enhance colloidal transport stems from its negative charge. Different adsorption configurations of HA result in varying modifications of surface properties. In this context, HA binds to the TPHs-SC surface in multiple orientations, thereby influencing the colloidal transport.

Recent advancements in quantum chemical calculations, first-principle calculations, molecular dynamics simulations, and ligand and charge distribution (LCD) models have significantly advanced the study of intermolecular structure calculations,[26] weak interactions,[34] changes in electrostatic potential profiles,[35] and colloidal aggregation and deposition.[36,37] Furthermore, these[36,37] calculations and simulations have elucidated the micro interface mechanisms governing colloid transport.[26,36−38] For example, the interactions between organic molecules and colloids[26] and the coordination modes of pollutants on colloid surfaces[36] can affect colloid transport. However, the impact of these factors on the surface potential of TPHs-SC and their transport, particularly when various organic compounds, such as TPHs and HA are present on colloid surfaces, remains unclear.

This study investigated the influence of HA on the transport of TPH-contaminated SC in porous media. Interfacial interactions among SC, TPHs, and HA were characterized by using aggregation and column experiments, transport simulations, extended Derjaguin−Landau−Verwey−Overbeek (XDLVO) theory, quantum chemical calculations, first-principle calculations, molecular dynamics simulations, and LCD models. The findings of this research contribute to a deeper understanding of the transport mechanisms of organic-contaminated SC.

■ MATERIAL AND METHOD

Preparation of SC. Soil samples were collected from the Binhai New District of Tianjin City, China, at coordinates 117°29′14.4″E, 38°48′52.9″N. Since the sampling site was near an oil mining area, the soil contained trace amounts of TPHs. Crude oil was supplied by the Oil Corporation. To prepare TPH-contaminated soil, 30 g of crude oil was added to 500 g of soil, which was then aged for one month. Both soil types were freeze-dried, ground, and passed through a 0.074 mm nylon sieve to remove large particles and ensure the mobility of the soil colloids. Details and results of the HA adsorption experiments conducted on the soil are provided in Supporting Information (SI) S1. However, due to interference from a significant amount of desorbed TPHs with the total organic carbon (TOC) determination, the HA adsorption experiment on TPH-contaminated soil was unsuccessful.

SC suspensions were prepared by adding 2.5 g of soil sample to 500 mL of Milli-Q water, followed by homogenization through stirring and sonication for 60 min. After settling for 24 h, the suspension was recovered by siphoning. For the TPH-contaminated soil, desorbed TPHs from the suspension surface were discarded. The samples were labeled SC and TPHs-SC, respectively. The concentration of colloid suspension was determined by measuring the absorbance at 420 nm using a spectrophotometer (TU1810, PGENERAL) (Figure S2), based on linear calibration curves correlating absorbance with standards.[12,39] The total elemental concentrations of Fe, Mn, Al, and Ca in the soil, SC, and TPHs-SC were measured by using inductively coupled plasma optical emission spectrometry (ICP-OES, Optima 5300DV, PerkinElmer) after digestion (Table S2). The same samples were analyzed for TOC using a TOC analyzer (Aurora 1030C, OI Analytical). The TPH content and fractions in the contaminated soil were extracted via ultrasonic and chromatographic leaching methods and quantified by using the weighing method. Additionally, clay minerals in the soil were identified by using X-ray diffraction (XRD, SmartLab SE, Rigaku). Infrared spectra of the TPHs, SC, and TPHs-SC were analyzed by using a Fourier infrared spectrometer (FTIR, Nicolet iS20 Thermo, Scientific). The micromorphologies of SC were observed with scanning electron microscopy (SEM, MIRA LMS, and TESCAN), complemented by line scanning energy-dispersive spectroscopy (EDS).

Aggregation Experiments. The changes in colloidal particle sizes of SC and TPHs-SC (20 mg L^{-1}) at varying HA^{-1}concentrations in NaCl or $CaCl_2$ solutions under pH 8.5 were measured using a dynamic light scattering analyzer (Zetasizer Nano ZS, Malvern Instruments). Hydrodynamic diameters (D_h) were recorded every 30 s for 20 min. Samples were measured in triplicate for each experiment.

Column Experiments. Column experiments were conducted using 10 cm long glass chromatographic columns with an inner diameter of 1.5 cm. The columns were wet-packed with clean quartz sand (337.5 μm) and goethite (GT)-coated quartz sand to simulate pore conditions in soil or aquifers. The effective porosity and bulk density of the packed sand were 0.46 ± 0.03 cm^3 cm^{-3} and 1.45 ± 0.02 g cm^{-3}, respectively.[26] After packing, the columns were preconditioned with approximately 15 pore volumes (PVs) of 1 mM NaCl in Milli-Q water using a peristaltic pump (BT-100 1F, Longer) in up-flow mode.

For all column experiments, 10 PVs of colloids (SC and TPHs-SC, 20 mg L^{-1}) at pH 8.5 with varying ionic strength (IS) and HA concentrations were injected into the columns, followed by elution with 10 PVs of Milli-Q water adjusted to the corresponding pH and IS, or pure Milli-Q water. The flow rate was maintained at a constant Darcy velocity of 0.568 cm min^{-1}. The particle deposition rate in up-flow mode was greater than that in down-flow mode.[40] The experimental conditions are summarized in Table S3. To simulate real-world conditions, IS and HA concentrations were changed in the experiment. Colloid concentrations in the effluent were measured at every half PV. In select transport experiments, the TPH concentrations (dissolved and total) in the effluent were measured for every three PVs using an infrared oil meter (OIL-460, CHINAINVENT) following carbon tetrachloride extraction. The particle size and ζ potential of the colloids, as

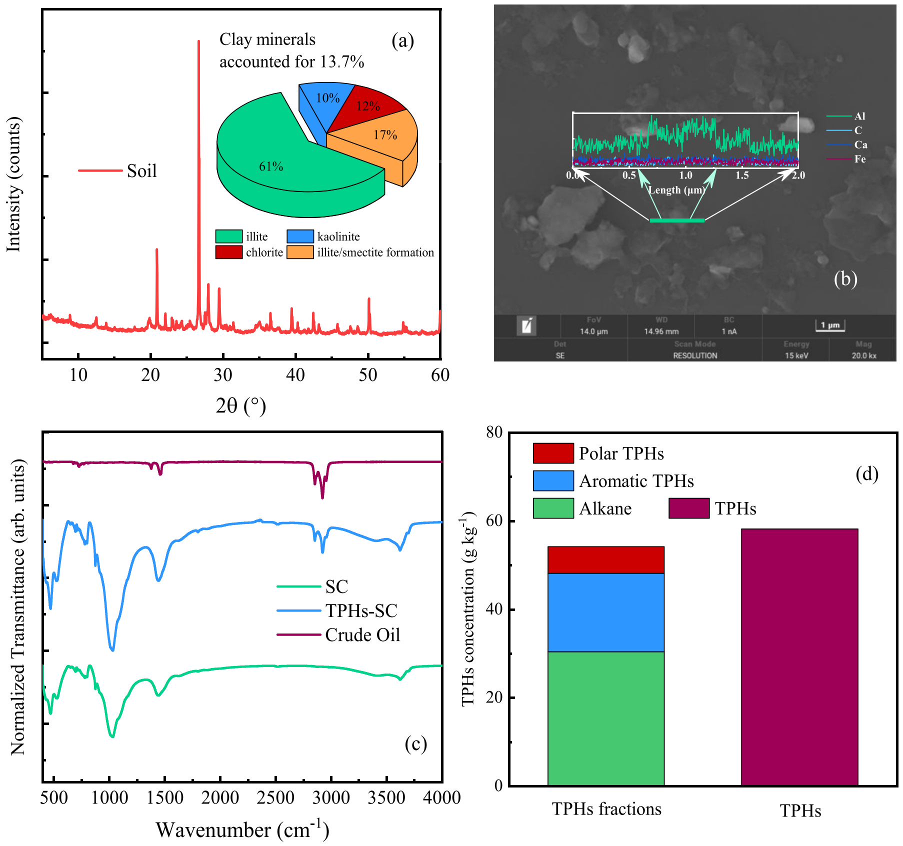

Figure 1. Quantitative clay mineral analysis of soil based on X-ray diffraction (a). SEM and EDS line scanning results for SC (b). Fourier infrared analysis of crude oil, SC, and TPHs-SC (c). Content and fraction of TPHs in TPH-contaminated soil (d).

well as the ζ potential of the sand, were determined under different conditions using a dynamic light scattering analyzer with results presented in Tables S4 and S5.

Model and Calculation. *Aggregation Model.* The initial aggregation rate constants (k) of colloids were proportional to the increasing rate in D_h over time.[41] The attachment efficiency (α) was determined as the initial rate of colloid aggregation and normalized based on the rate of aggregation under diffusion-limited conditions.[41] The details of the colloid aggregation models are provided in SI S6.

Transport Model. A conservative tracer can be used to monitor the hydraulic characteristics of the columns. Since the column, sand, and filling methods are consistent with those used in previous studies, the hydraulic characteristics of the column are cited from previous studies.[26,42] The transport data were simulated using the colloid transport model, which incorporated two-site kinetic retention to quantify the transport and retention of colloids in the column experiments.[43,44] The details of the colloid transport models are provided in SI S7.

DLVO and XDLVO Theory. The Derjaguin−Landau−Verwey−Overbeek (DLVO) and extended DLVO (XDLVO) theories were used to calculate the total colloid-sand interaction energy.[45,46] The details of the DLVO and XDLVO theories and the operative equations are presented in SI S8.

Quantum Chemical Calculation. To investigate the intricacies of TPHs-HA interactions, representatives of alkanes, aromatic hydrocarbons, and polar TPHs were selected. The molecular formulas of *n*-decane, naphthalene, naphthenic acid, and HA are shown in Figure S14. Quantum chemistry calculations are challenging to perform on large molecular models; therefore, the Stevenson HA model with 160 atoms was chosen. A range of software, including the Molclus program,[47] Gaussian 16, and Multiwfn,[48] were used to optimize the cluster configuration and calculate the interaction energy and weak interactions. The details of the quantum chemical calculations are presented in SI S9.

First-Principle Calculation. The calculations were based on the density functional theory under periodic boundary conditions, as implemented in the CP2K/Quickstep package.[49] The hybrid Gaussian and plane wave method was used to treat the ion-electron interactions.[50] The vdW correction was applied using the Grimme approach.[51] Additional details of the first-principles calculations are presented in SI S10.

Molecular Dynamic Simulation. Dynamic simulations of TPHs and HA on Illite (001) were performed using the GROMACS 2021 software package.[52−54] A universal force field[55] was used to parametrize all the atoms of Illite, and the OPLSS-AA force field[56] was used to parametrize the TPHs and HA molecules. The molecular dynamics (MD) simulation were performed in an NVT ensemble with a simulation time of 50 ns. In the NVT simulations, the V-rescale thermostat maintained a temperature of 298.15 K. Additional details of the MD simulations are presented in SI S11.

LCD Model. The LCD model was employed to calculate the adsorption of HA and the potential changes under different HA adsorption conformations. The extended Stern model was used to describe the potential structure. The LCD model considers the spatial distribution of HA within the diffuse double layer (DDL), including the inner layer (Stern layer) and the outer layer (diffuse layer). The site density, as well as

https://doi.org/10.1021/acs.est.4c11233
Environ. Sci. Technol. XXXX, XXX, XXX−XXX

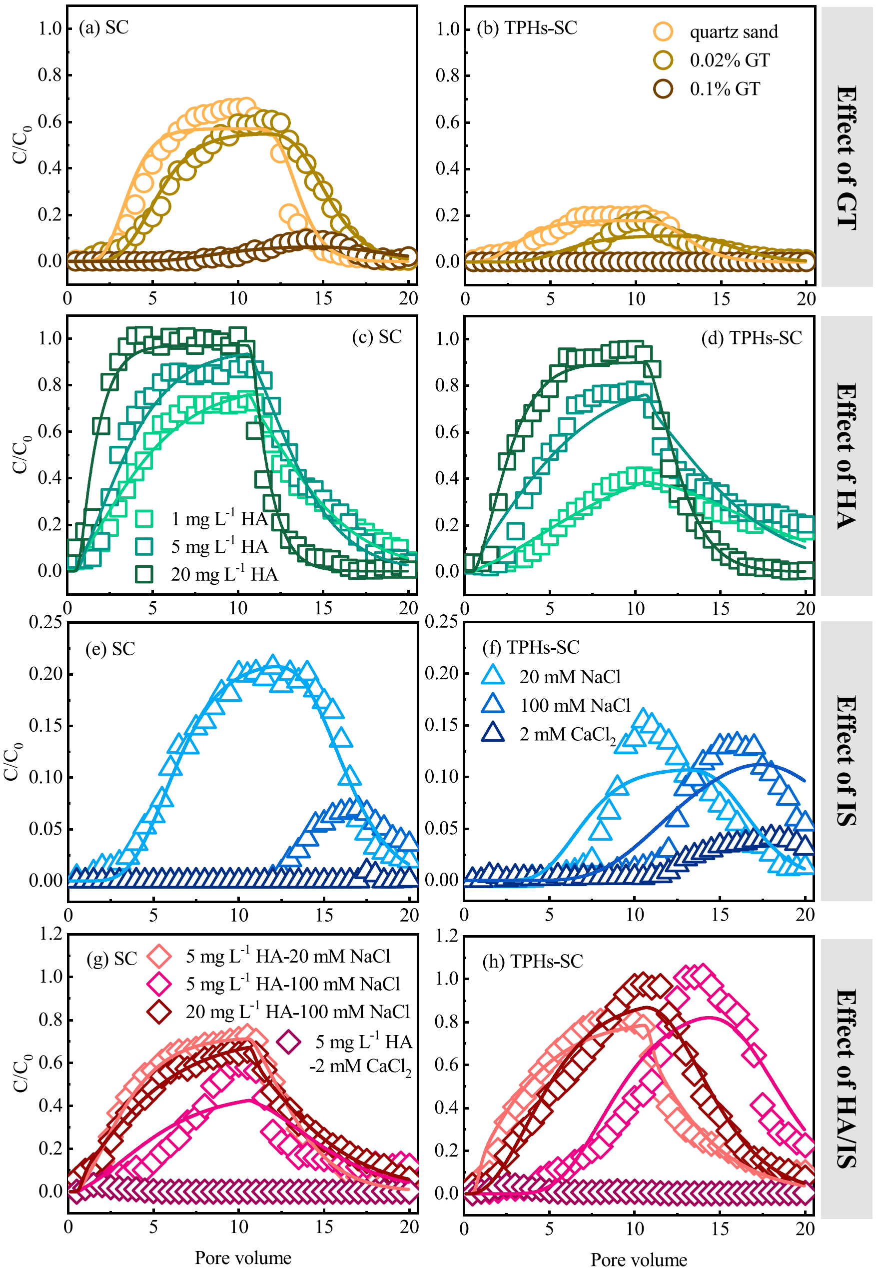

Figure 2. Breakthrough curves of the transport of SC (a, c, e, and g) and TPHs-SC (b, d, f, and h) at an influent pH of 8.5 in the quartz sand and GT-coated sand columns (a, b) with different concentrations of HA in the 0.02% GT-coated sand columns (c, d), different IS in the 0.02% GT-coated sand columns (e, f), and various concentrations of HA and IS in the 0.02% GT-coated sand columns (g, h). Symbols indicate observed data and solid lines indicate simulation fitting. Recovery rates of <5% in the effluent did not fit.

the inner and outer layer capacitance, were assumed to be the same as kaolinite.[57] The theory and framework of the LCD model have been detailed in a previous study.[58] For more information about the modeling, please refer to SI S12.

■ RESULTS AND DISCUSSION

Physicochemical Properties of soil and SC. The soil primarily consisted of quartz (41.8%), plagioclase (26.0%), clay minerals (13.7%), potassium feldspar (8.5%), and calcite (8.0%) (Figure S3), with a relatively high content of clay minerals, Illite (61%) and other clay minerals, including kaolinite, chlorite, and Illite/smectite formations (10−17% each) (Figure 1a). SEM results revealed that the particle sizes of SC and TPHs-SC ranged from 330 to 760 nm (Figure S4). EDS line scanning indicated a high aluminum content in TPHs-SC due to the abundance of Illite in the soil (Figure 1a), suggesting that Illite is the dominant mineral in the SC.

Crude oil primarily consists of hydrocarbon compounds but also contains a small amount of nonhydrocarbon compounds and asphaltenes. The proportions of N and S in the crude oil were 0.39 and 0.31%, respectively. In the infrared spectrum of crude oil, stretching vibration absorption peaks of methyl and methylene groups were observed at 2853 and 2954 cm^{-1}, while bending vibration absorption peaks of methyl and methylene appeared at 1377 and 1457 cm^{-1}, indicating the presence of straight-chain alkanes and cycloalkanes. The absorption band at 1028 cm^{-1} in the infrared spectrum of SC (Figure 1c) corresponds to the in-plane Si−O stretching vibration, partly attributed to the absorption of Illite in the SC.[59] The FTIR spectra of TPHs-SC showed notable TPH peaks (2853 and 2954 cm^{-1}), confirming the adsorption of TPHs on TPHs-SC (Figure 1c). In the TPH-contaminated soil, the TPH concentration was 58.2 g kg^{-1}, with alkane, aromatic hydrocarbon, and polar TPHs accounting for 56.2, 32.7, and 11.1%, respectively (Figure 1d), suggesting considerable TPH adsorption on the surface of soil particles.

Aggregation of SC and TPHs-SC. The concentrations of SC and TPHs-SC did not affect their stability (Figure S5). This study was conducted under a constant pH of 8.5 to simulate the alkaline soil conditions[60] in the sampling area, which had a pH buffer in the soil solution for soil pore water and groundwater. The change in colloidal particle size over time was measured in solutions of NaCl (0−1000 mM) and $CaCl_2$ (0−600 mM) with and without the presence of humic acid (HA), as shown in Figures S6−S9. Additionally, the aggregation rates (k) and attachment efficiency (α) of SC and TPHs-SC are illustrated in Figure S10. The k values for SC and TPHs-SC increased as the ionic strength (IS) rose, surpassing 500 mM NaCl and 10 mM $CaCl_2$ (Figure S10a,b). Below the critical coagulation concentration (CCC), the hydrodynamic diameter (D_h) gradually increased with electrolyte concentration, indicating an increase in α (Figure S10c,d). Furthermore, the CCCs observed in $CaCl_2$ solutions were consistently lower than those in NaCl solutions due to $CaCl_2$'s stronger compressive effect on the electrical double layer and superior charge neutralization capabilities compared to NaCl.[61]

Under high concentrations of NaCl (400−1000 mM), the average k values of SC-5 mg L^{-1} HA increased by 1.24 times compared to those without HA. Similarly, the average k values of SC-20 mg L^{-1} HA increased by 2.59 times compared to the low HA concentration (Figure S10a). For TPHs-SC, the k values increased by 1.21 and 2.08 times with an increasing HA concentration (Figure S10a). The increase factors under high $CaCl_2$ conditions were 2.50 and 1.79 for SC, and 2.44 and 1.50 for TPHs-SC (Figure S10b). The increase in k values for TPHs-SC was consistently lower than for SC. Additionally, in the presence of HA, the CCCs of TPHs-SC (917.3−929.7 for NaCl and 69.2−69.4 for $CaCl_2$) were higher than those of SC (870.2−926.2 for NaCl and 60.2−67.4 for $CaCl_2$) (Table S6). Illite, the main component of the SC in this study, exhibited a relatively weak CEC and a thick double-electron layer.[62] Although Illite carries a lower negative charge, it can maintain the stability of the colloid at low IS. The adsorption of TPHs did not change their stability, and HA improved the colloidal stability at low IS. However, HA increased the ion-bridging effect at high IS values.[63] Combined with the k and CCC values, the destabilizing effect of HA in the SC system was stronger than that in the TPHs-SC system.

Transport of Colloids and TPHs. *Effect of GT on the Transport of SC and TPHs-SC.* The transport of SC and TPHs-SC in water-bearing media was examined. To clarify, the dispersivity of colloids is size-dependent,[64] and the size of the soil colloids tends to increase (Figures S6−S9). Thus, the dispersivity used in this study is likely underestimated. It was found that transport decreased with increasing GT content (from 0 to 1%), leading to a significant reduction in the recovery rate (Figure 2a,b and Table S7). This GT-induced retardation of colloid and nanoparticle transport has been widely reported in previous studies.[7,26] The deposition of TPHs-SC was more evident than that of SC, indicating that quartz sand and GT, with their amphoteric oxidation characteristics, tended to adsorb TPHs-SC. However, the recovery rate of SC sharply decreased (from 54.76 to 5.57%), suggesting that SC was more sensitive to the change in the collector from quartz to GT-coated quartz than TPHs-SC. Retention primarily occurred at reversible sites, corresponding to high k_{1a} and low k_{2a} values (Table S7).

Effect of HA on the Transport of SC and TPHs-SC. The transport of SC and TPHs-SC was enhanced by HA, with the enhancement becoming more pronounced as the concentration of HA increased (Figure 2c,d). This was due to the negative charge of HA after its adsorption on the colloid.[7,24,26,28,65,66] The increasing transport speed narrowed the gap in transportation ability between SC and TPHs-SC, leading to a decrease in the discrepancy of recovery rates from 37.59 to 7.86% (Table S7). This trend may be attributed to the more negative potential that HA provided on TPHs-SC (−28.5 to −34.0 mV) compared to SC (−25.2 to −29.5 mV) (Table S4). Although SC transport remained faster than that of TPHs-SC, the impact of HA on enhancing TPHs-SC transport was more significant. This observation aligns with the finding that TPHs-SC exhibited less aggregation than SC in the presence of HA (Figure S10). The higher amount of HA adsorbed on the colloid led to a more negative potential on the colloid surface. However, due to TPHs occupying some adsorption sites on TPHs-SC, it is speculated that the amount of HA adsorbed on TPHs-SC did not exceed that on SC. Consequently, the negative potential on TPHs-SC was higher than that on SC, contradicting previous hypotheses.

Effect of IS on the Transport of SC and TPHs-SC. The IS significantly impacts colloidal transport. This study observed that the transport rates of SC and TPHs-SC were influenced by IS conditions (Figure 2e,f). Specifically, at low monovalent cation concentrations (20 mM NaCl), SC transport was faster than TPHs-SC transport. However, as the IS increased to 100 mM (NaCl) or in the presence of bivalent cations (2 mM $CaCl_2$), the TPHs-SC transport exceeded SC transport. These findings indicate that IS delays the transport of SC more than TPHs-SC. These results suggest that IS has a minimal effect on the double-electron shell compression of TPHs-SC due to hydrophobic layer interference.

Effect of HA under the IS on the Transport of SC and TPHs-SC. The presence of HA counteracted the retarding effect of monovalent cations (Figure 2e−h) on the transport of TPHs-SC, resulting in a higher recovery (44.31−89.07%) compared to that without HA (3.84−21.43%) (Table S7). In the presence of monovalent cations and HA, TPHs-SC transport was faster than that of SC (Figure 2g,h). However, the recovery of TPHs-SC was slightly lower than that of the HA-TPHs-SC system, suggesting that HA plays a stronger role in promoting TPHs-SC transport under specific IS conditions. This effect is attributed to the difference in ζ potential, with TPHs-SC having a lower average negative ζ potential (−29.8 mV) than SC (−28.1 mV) (Table S4). The different adsorption of HA on the two colloids may explain this discrepancy. Nevertheless, the presence of HA did not reverse the low transport of the colloids under bivalent cation ($CaCl_2$) conditions (Figure 2g,h), as Ca^{2+} has a stronger ability to compress the double-electron layer, leading to increased colloid deposition by facilitating ion-bridging interactions.[67]

Colloidal Release due to HA and IS Reduction. The release capacity of colloids in water-bearing media depends on the interaction between colloids and sand as well as the reversibility of deposition. Following the elution phase of SC

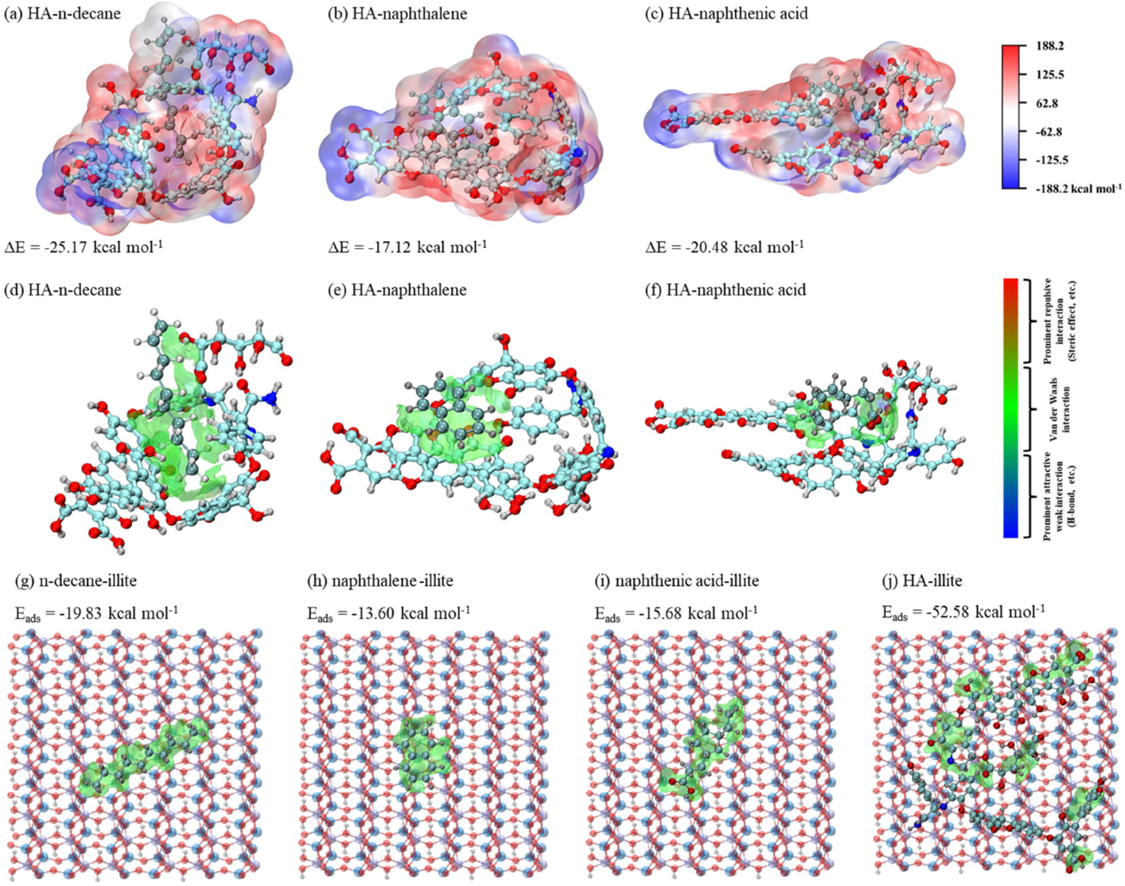

Figure 3. ESP-mapped van der Waals surfaces of HA-TPHs (a−c); ESP denotes the electrostatic potential of the molecule, wherein red and blue are the positive and negative areas, respectively. Visualized weak interaction regions of IGMH (isolevel 0.002) with different perspectives of HA-TPHs (d−f) and TPHs/HA-Illite (001) surfaces (g−j). The definition of IGMH does not involve electrostatic interactions. C, H, O, N, Si, and Al are labeled using cyan, white, red, blue, dark blue, and light purple, respectively. HA molecules, TPH molecules, and Illite crystal structures use different mage-rendering methods.

or TPHs-SC, the columns were flushed with Milli-Q water at pH 8.5 to promote colloid remobilization. Prominent peaks were observed under different IS and HA conditions (Figures S11 and S12), differing from those observed under normal conditions. Regardless of the presence of HA, a sharp transient peak appeared, particularly pronounced under monovalent cation conditions. HA increased the peak to a higher height.

Cotransport of TPHs with TPHs-SC. The transport ability of total and colloid-adsorbed TPHs under different conditions followed the same pattern as that of TPHs-SC (Figures S13a,c, and 2), showing strong positive correlations (R^2 = 0.752, p < 0.01 and R^2 = 0.771, p < 0.01, respectively) with the relative concentration of TPHs-SC (Figure S13d,f). This observation suggests the cotransport of TPHs with TPHs-SC. Dissolved TPH transport was minimal in the absence of HA (Figure S13b), indicating that HA induced dissolved TPH transport. The concentrations of dissolved TPHs showed a weak positive correlation (R^2 = 0.403, p < 0.01) with the relative concentration of TPHs-SC (Figure S13d). Therefore, the possibility that colloid-adsorbed TPHs are released during transport cannot be disregarded. Under hydrodynamic or HA competitive adsorption, a certain proportion of TPHs can be removed from the surface of the TPHs-SC and adsorbed onto quartz sand surfaces, subsequently impacting TPHs-SC transport. The release of TPHs is related to the competition for HA on the colloidal surface. Thus, the interactions between HA, TPHs, and colloids must be further investigated.

Interaction among HA, Typical TPHs, and Illite. Quantum chemical calculations were conducted to further investigate the molecular-scale interactions between HA and the typical TPHs. The electrostatic potential of van der Waals surfaces (ESP) of the molecules is shown in Figure S14. The surface potential distributions (positive and negative regions) of HA, naphthalene, and naphthenic acid were uneven, with polar surface areas of 665.1 (65.0% of the molecular surface area), 101.2 (58.3%), and 89.2 (38.3%) Å^2, respectively. Although *n*-decane is a nonpolar molecule, the binding energy between HA and *n*-decane (−25.17 kcal mol^{-1}) was stronger than those of the HA-naphthalene (−17.12 kcal mol^{-1}) and HA-naphthenic acid (−20.48 kcal mol^{-1}) systems (Figure 3a−c). Additionally, noncovalent interactions, including prominent attractive weak interactions, van der Waals interactions, and prominent repulsive interactions,[68] were analyzed using the independent gradient model based on the Hirshfeld partition (IGMH, δg^{inter}) between HA and typical TPHs (Figure 3d−f). The chain-like *n*-decane was embedded in the HA molecule, and E_{VdW} was observed between them as the main weak interaction (Figure 3d and S16a). The chain molecules have large contact areas with HA, resulting in strong interactions.[26] The benzene rings of naphthalene facilitated $\pi-\pi$ interactions in the HA-naphthalene system (Figure 3e), which constitute a

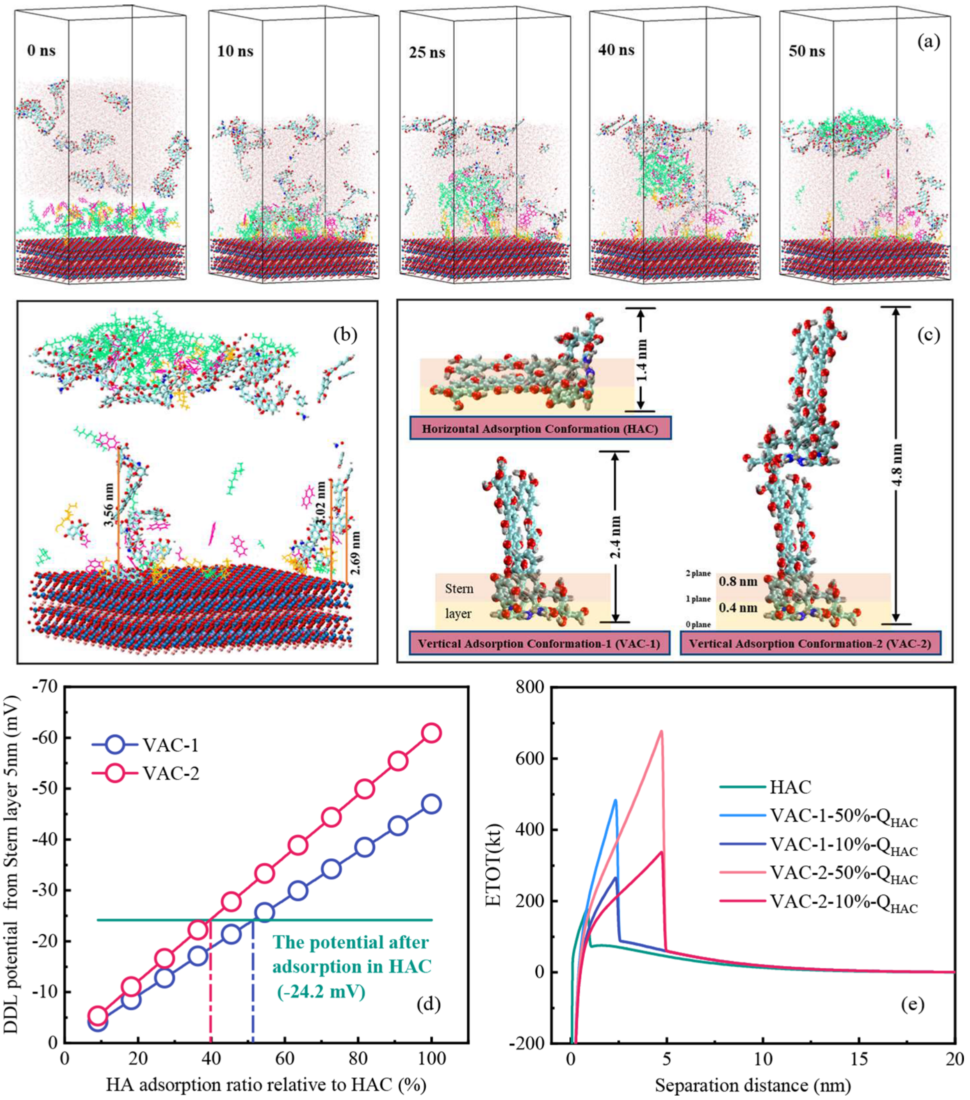

Figure 4. Representative snapshots of the adsorption of HA to TPH-contaminated colloids (a); the detailed point-in-time snapshots are shown in Figure S18. The *n*-decane, naphthalene, and naphthenic acid molecules are distinguished by green, light red, and yellow lines, respectively. The HA and Illite are labeled using the Corey−Pauling−Koltun method. The water molecules are labeled using the point method. Models of different HA adsorption configurations (c). Scenario analysis of colloidal DDL potential (d) and extended DLVO theory (e) under different HA adsorption configurations and adsorption quantities.

class of noncovalent interactions,[69] with van der Waals interactions playing a central role (Figure S16b). Due to the hydroxyl group, naphthenic acid formed an H-bond with the oxygen on HA (Figure 3f, light blue area). This is also reflected in the corresponding IGMH scatter plot, where blue dots appear in the negative position of sign(λ_2)ρ (Figure S16c). Different types of TPHs interact with HA in various ways, and it is expected that the interaction between TPHs and HA will become more intense as the chain length, aromatic rings, and polar groups of the TPH molecules increase.

According to the results of the first-principles calculations, no chemical bonds were formed between the TPHs/HA and Illite, indicating that their adsorption on the 001 Illite surface primarily occurs via physisorption (Figure 3j−m). The adsorption energies of *n*-decane, naphthalene, and naphthenic acid on Illite were −19.83, −13.60, and −15.68 kcal mol^{-1}, respectively (Figure 3g−i). The adsorption energy between HA and Illite (−52.58 kcal mol^{-1}) (Figure 3j) was much higher than those of the other interactions. This suggests that HA adsorption onto Illite has a significant advantage over competitive adsorption. Kaolinite and chlorite are also common components of soil colloids. Illite, kaolinite, and chlorite are similar in elemental composition (Si, Al, and O) and have a layered structure, which may contain cations between the layers to balance the layer charges. Therefore, the interaction of TPHs/HA is similar to that of these three typical clay minerals. The adsorption energy obtained by the two calculation methods cannot be accurately compared due to the inconsistency of the calculation systems. However, the small energy gaps between TPH adsorption on Illite and the binding of TPHs to HA (5.34 kcal mol^{-1} for *n*-decane, 3.52 kcal mol^{-1} for naphthalene, and 4.80 kcal mol^{-1} for naphthenic acid, respectively) (Figure 3a−c, g−i) suggest that competitive adsorption in the system is complex. Therefore, we speculate that HA can initiate dynamic exchanges with the TPHs on the Illite surfaces.

The TPH molecules adsorbed on the 001 surface in a relatively stable horizontal conformation (Figure S15a−c). HA can fold into a three-dimensional conformation due to its flexibility (Figure S15d). One part of the molecule forms a strong vdW attraction with Illite (Figure S17), while another part protrudes from the surface. The O atoms in the carbonyl group of the benzene ring were as high as 0.98 nm (Figure S15d), which exceeded the thickness of the two-plane in the Stern layer (0.8 nm) defined by the CD-MUSIC model.[70] Moreover, the distances between the O atoms in the phenolic hydroxyl or carboxyl group and the mineral surface ranged from 0.49 to 0.72 nm (Figure S15d), which is higher than the thickness of the one-plane in the Stern layer (0.4 nm). Under alkaline conditions, the carbonyl group on the outermost layer of the colloidal surface (Figure S17) may become deprotonated and negatively charged, further enhancing the colloidal transport. However, the competitive adsorption and interaction of multiple TPHs and HA molecules are complex, and the adsorption kinetics of HA onto TPHs-SC needs further investigation.

Effect of Adsorption Conformation on the Transport of Colloids and TPHs. This study investigated the adsorption of HA on contaminated colloids and its competitive adsorption with representative TPHs by using MD simulations. Initially, TPH molecules were randomly distributed on the 001 Illite surface, creating a hydrophobic layer near the colloidal surface (Figure 4a). From 0 to 5 ns, most TPHs aligned horizontally with the Illite surface (Figure S18b) to minimize energy, consistent with the first-principles adsorption conformation (Figure 3g−i). Upon interaction with HA, the hydrophobic layer was disrupted (∼10 ns), causing the average center of geometry (COG) distance between HA and Illite to decrease (from 6.98 to 4.91 nm) before slightly increasing (up to 6.11 nm; Figure S19a). This is primarily because the hydrophobic TPHs adsorbed by HA-repelled surrounding water molecules[71] which carried HA to the top of the water interface (Figure 4a). The average electrostatic and vdW interactions between TPHs/HA and Illite fluctuated considerably from 0 to 10 ns (Figure S19c), suggesting vigorous competitive adsorption between HA and TPHs on the surface. Subsequently, the COG distance between the hydrophobic TPHs (*n*-decane and naphthalene) and Illite increased progressively due to competition for HA adsorption (Figure S19a).

At the end of the simulation, some HA molecules, along with a large amount of naphthenic acid (67.7%), 30% naphthalene, and a minority of *n*-decane (8%), were attached to the Illite surface. The electrostatic interactions stabilized HA and naphthenic acid on the Illite surface (Figures 4b and S19c). Molecules near the Illite surface, predominantly naphthalene and naphthenic acid, were adsorbed by HA and bonded weakly (Figure 4b). This weak interaction caused another HA component to form heteroaggregates with TPHs (mainly *n*-decane) in the water phase. Due to the volume limitation in the simulation box, the heteroaggregated HA infiltrated the water phase, with TPHs oriented outward (Figure 4b). In the saturated state, the heteroaggregated supramolecules were dispersed in the aqueous phase, existing in a dissolved or colloidal state rather than at the gas−liquid interface. Overall, the coexistence of HA and TPHs on the Illite colloid surface resembled the zonal model. Polar HA and naphthenic acid interacted with the colloidal surface, and their hydrophilic parts were exposed to the aqueous phase.[22] The difference was that the hydrophobic zone was not in the outer layer of the contact zone; instead, it partially coincided with the contact zone under the constraints of a weak interaction, making it appropriate to call this the weak interaction zone. In the kinetic zone, HA, TPHs, and heteroaggregated supramolecules dispersed in the aqueous phase can be adsorbed onto colloids again under certain conditions.

First-principles calculations and MD simulations of HA adsorption onto noncontaminated Illite (Figures S17 and S20) showed that HA adopts a horizontal adsorption conformation to reach the lowest energy state of the system, forming a negative potential region on the surface (Figure S17), which promotes colloid transport. In the MD simulation of HA adsorption onto TPH-contaminated Illite, the HA adsorption conformation was more diverse because the hydrophobic TPHs occupied a large number of adsorption sites. HA that adsorbed vertically onto Illite.[72] TPHs in the weak interaction zone may have contributed to the fixation of the vertical adsorption conformation. The vertically adsorbed HA stacked in such a way that the functional groups of some vertically adsorbed HA peaks reached 2.56−3.69 nm from the Illite surface (Figure 4b), which is 2.6−7.5 times greater than those of horizontal adsorption (0.49−0.98 nm), protruding beyond the Stern layer.

According to the calculation results, we assumed three adsorption conformations: horizontal adsorption (HAC), vertical adsorption (VAC-1), and vertical adsorption of two HA stacks (VAC-2) (Figure 4c). The three-dimensional size of HA was calculated based on quantum chemistry results (Figure S14a). Given the reduced vertical adsorption of HA, scenario analysis of DDL potentials and XDLVO energies was conducted (Figure 4d,e). According to the LCD model results, the adsorption capacities of HA in VAC-1 and VAC-2 were 51 and 40% of the HAC adsorption capacity, respectively. The DDL potentials for VAC-1 and VAC-2 were similar to those of HAC (−24.2 mV) (Figure 4d). The calculated DDL potential for HAC was close to the measured ζ potential of SC (−25.2 to −29.5 mV; Table S4), demonstrating the applicability of the LCD model. Therefore, the vertical adsorption conformation facilitated the transfer of negative potential to the DDL, resulting in a more negative potential on the TPHs-SC (−28.5 to −34.0 mV; Table S4).

From the perspective of DLVO theory, the vertical adsorption conformation increased the Debye length (and decreased the Debye−Hückel parameter), which led to an increase in the DLVO energies between the TPHs-SC and the GT-coated sand. The DLVO energies in the TPHs-SC system were consistently higher than those in the SC system (Figures S22 and S23). Furthermore, the vertical adsorption conformation generated larger osmotic and elastic-steric repulsion forces (Figure 4e). Under competitive adsorption of TPHs, even a small amount of vertically adsorbed HA (10%) on contaminated colloids produced a larger energy barrier (272.0 kt for VAC-1 and 342.6 kt for VAC-2) compared to horizontal adsorption (185.6 kt; Figure 4e). Due to electrostatic interactions, osmotic repulsion, and elastic-steric repulsion between colloids and collector drives, vertically adsorbed HA significantly enhanced colloid transport. Moreover, the protruding HA's phenolic hydroxyl or carboxyl groups were readily deprotonated at alkaline pH, forming a strong negative charge that delayed colloid aggregation and promoted colloid transport.

Colloid-adsorbed and dissolved TPHs coexisted during the transport experiments. Colloid-adsorbed TPHs originated from the contact and hydrophobic zones, while dissolved TPHs came from the dynamic zone or solutions far from the colloids. The TPHs in the kinetic zone may be adsorbed or released from the colloids during transport; thus, there is a correlation between dissolved TPHs and the colloid (Figure S13e). Goethite has a strong adsorption capacity for dissolved organic matter (DOM),[26] which retards the transport of dissolved TPHs. Therefore, in this study, the TPH concentrations in the effluent were low (Figure S13b). In the TPHs-SC, the hydrophobic layer prevented the proximity of water molecules and ions, reducing the chance that ions react with the surface of the colloid. As a result, the column experiment showed that IS retarded the transport of SC to a greater extent than did TPHs-SC. When HA was involved, the hydrophobic layer on the TPHs-SC was destroyed. HA was vertically adsorbed to form an adsorption conformation, which facilitated negative potential transfer and partially counteracted the effect of a double electric layer compression. For the SC surfaces where HA was horizontally adsorbed, this counteracting effect was not evident. This caused HA to enhance the transport of TPHs-SC more significantly than SC. In the presence of HA, the TPHs-SC deposited on the collector were readily affected by hydraulic scouring or changes in environmental conditions and were released into the water phase again.

The MD simulation employed three representative TPHs, selected based on their fractions in the contaminated soil. In real-world environments, counting and simulating all types of TPH molecules is challenging. Fortunately, the molecular properties of each TPH class are similar,[73] making the simulation representative. In slightly oil-contaminated soils, TPHs are unlikely to fully cover the colloidal surface. However, if TPHs occupy enough adsorption sites to disrupt the horizontal adsorption of HA, then HA dominates the formation of the zonal model on TPHs-SC. This can still result in enhanced colloid transport.

■ ENVIRONMENTAL IMPLICATIONS

Although sustainable alternatives to petroleum are being developed, they remain a cornerstone of the global economy and are widely used in transportation, industry, and daily life. Petroleum exploitation, however, contributes to soil and groundwater pollution through the release of TPHs. SC plays a critical role in the transport of TPHs. Many oil-contaminated sites are located near forests[74] and farmland,[75] whereas others are located on the coast[76] or near rivers and lakes.[77] In these regions, soil and aquifer conditions vary in different regions with organic matter, ions, and water conditions in soils and aquifers changing frequently. Organic matter enhances the colloidal transport. This study proposes a novel mechanism in which HA dominates the zonal model on TPHs-SC and enhances colloidal transport via vertical adsorption. Sites near forests and farmland often have higher organic matter content, and macromolecular DOM with a nongeometric three-dimensional conformation may form vertical adsorption conformations on SC. These conformations delay TPHs-SC aggregation and promote TPH diffusion. In coastal or salinized soils, Na^+ in pore water does not inhibit TPHs-SC transport. In regions near rivers and lakes, DOM affects hydraulic conditions and facilitates the rerelease of colloidally adsorbed TPHs. Iron oxide colloids are prevalent in iron-rich soils, and their interactions with TPHs and HA may differ from those involving clay minerals, warranting further investigation. Additionally, existing cotransport models have been developed[78,79] and should be applied in future research.

■ ASSOCIATED CONTENT

Supporting Information

The Supporting Information is available free of charge at https://pubs.acs.org/doi/10.1021/acs.est.4c11233.

> Adsorption experiments of HA on soil; calibration curves of concentrations of colloids; chemical analysis and characteristics of soil and colloid; column experiments condition; zeta potential and particle size of experimental materials; colloid aggregation models; colloid transport models; S8. DLVO and XDLVO theory; quantum chemical calculation; first principle calculation; molecular dynamics simulation; LCD model theory; major mineral components of soil; particle size distribution of soil colloid; effect of colloid concentration on the aggregation of colloid; change of colloidal particle size with time in NaCl and $CaCl_2$ solution with and without the presence of HA; aggregation of oil colloid and TPH-contaminated colloids; critical coagulation concentration of colloids; fitted parameters of soil colloids transport in the columns; effect of hydraulic action on colloidal release; cotransport of TPHs with TPH-contaminated colloids; conformation and characteristics of HA and TPHs molecules; visualized weak interaction regions of the TPH/HA-Illite (001) surface; IGMH scatter maps; ESP-mapped van der Waals surfaces of adsorbed HA on Illite (001); molecular dynamics simulation of the adsorption of HA to TPH-contaminated colloids; molecular dynamics simulation of the adsorption of HA to soil colloids; and DLVO results (PDF)

■ AUTHOR INFORMATION

Corresponding Authors

Jie Ma − *Agro-Environmental Protection Institute, Ministry of Agriculture and Rural Affairs, Tianjin 300191, China;* orcid.org/0000-0003-3404-6544; Email: majie@caas.cn

Haiming Li − *College of Marine and Environmental Science, Tianjin University of Science and Technology, Tianjin 300457, China;* Email: lhm@tust.edu.cn

Authors

Ping Zhou − *College of Marine and Environmental Science, Tianjin University of Science and Technology, Tianjin 300457, China*

Yong Liu − *Agro-Environmental Protection Institute, Ministry of Agriculture and Rural Affairs, Tianjin 300191, China*

Wanli Lian − *Agro-Environmental Protection Institute, Ministry of Agriculture and Rural Affairs, Tianjin 300191, China*

Bingcong Feng − *Agro-Environmental Protection Institute, Ministry of Agriculture and Rural Affairs, Tianjin 300191, China*

Li Li − *College of Marine and Environmental Science, Tianjin University of Science and Technology, Tianjin 300457, China*

Yujie Zhao − *Agro-Environmental Protection Institute, Ministry of Agriculture and Rural Affairs, Tianjin 300191, China*

Liping Weng − *Agro-Environmental Protection Institute, Ministry of Agriculture and Rural Affairs, Tianjin 300191, China; Department of Soil Quality, Wageningen University, 6700 AA Wageningen, The Netherlands*

Gangxing Lei – *Energy Conservation & Pollution Reduction Monitor Center, China National Offshore Oil Corporation, Tianjin 300452, China*

Complete contact information is available at:
https://pubs.acs.org/10.1021/acs.est.4c11233

Notes

The authors declare no competing financial interest.

■ ACKNOWLEDGMENTS

The study is financially supported by the National Natural Science Foundation of China (Nos. 42377409, 42072288, and 42377035), the Natural Science Foundation of Tianjin (23JCYBJC00310), and the Science and Technology Innovation Project of the Chinese Academy of Agricultural Sciences.

■ REFERENCES

(1) Wei, K. H.; Ma, J.; Xi, B. D.; Yu, M. D.; Cui, J.; Chen, B. L.; Li, Y.; Gu, Q. B.; He, X. S. Recent progress on in-situ chemical oxidation for the remediation of petroleum contaminated soil and groundwater. *Journal of Hazardous Materials* **2022**, *432*, No. 128738.

(2) Jabbar, N. M.; Alardhi, S. M.; Mohammed, A. K.; Salih, I. K.; Albayati, T. M. Challenges in the implementation of bioremediation processes in petroleum-contaminated soils: A review. *Environmental Nanotechnology, Monitoring & Management* **2022**, *18*, No. 100694.

(3) Park, I. S.; Park, J. W. A novel total petroleum hydrocarbon fractionation strategy for human health risk assessment for petroleum hydrocarbon-contaminated site management. *Journal of Hazardous Materials* **2010**, *179* (1−3), 1128−1135.

(4) Ugochukwu, U. C.; Chukwuone, N. A.; Jidere, C.; Agu, C.; Kurumeh, L.; Ezeudu, O. B. Legacy PAHs in effluent receiving river sediments near a large petroleum products depot in Enugu, Nigeria: Human health risks and economic cost of pollution. *Environ. Pollut.* **2022**, *309*, No. 119731.

(5) Lv, Y.; Bao, J.; Dang, Y.; Liu, D.; Li, T.; Li, S.; Yu, Y.; Zhu, L. Biochar Aerogel Enhanced Remediation Performances for Heavy Oil-Contaminated Soil through Biostimulation Strategy. *Journal of Hazardous Materials* **2023**, *443*, No. 130209.

(6) Honeyman, B. D. Colloidal culprits in contamination. *Nature* **1999**, *397* (6714), 23−24.

(7) Chen, Y.; Ma, J.; Wu, X.; Weng, L.; Li, Y. Sedimentation and Transport of Different Soil Colloids: Effects of Goethite and Humic Acid. *Water* **2020**, *12* (4), 980.

(8) Liu, F.; Xu, B.; He, Y.; Brookes, P. C.; Tang, C.; Xu, J. Differences in transport behavior of natural soil colloids of contrasting sizes from nanometer to micron and the environmental implications. *Science of The Total Environment* **2018**, *634*, 802−810.

(9) Zhou, D.; Wang, D.; Cang, L.; Hao, X.; Chu, L. Transport and re-entrainment of soil colloids in saturated packed column: effects of pH and ionic strength. *Journal of Soils and Sediments* **2011**, *11* (3), 491−503.

(10) Chen, J.; Zhang, H.; Wei, Q.; Farooq, U.; Zhang, Q.; Lu, T.; Wang, X.; Chen, W.; Qi, Z. Mobility of water-soluble aerosol organic matters (WSAOMs) and their effects on soil colloid-mediated transport of heavy metal ions in saturated porous media. *Journal of Hazardous Materials* **2022**, *440*, No. 129733.

(11) Li, Z.; Zhou, L. Cadmium transport mediated by soil colloid and dissolved organic matter: A field study. *Journal of Environmental Sciences* **2010**, *22* (1), 106−115.

(12) Ma, J.; Guo, H.; Lei, M.; Wan, X.; Zhang, H.; Feng, X.; Wei, R.; Tian, L.; Han, X. Blocking effect of colloids on arsenate adsorption during co-transport through saturated sand columns. *Environ. Pollut.* **2016**, *213*, 638−647.

(13) Barton, C. D.; Karathanasis, A. D. Influence of Soil Colloids on the Migration of Atrazine and Zinc Through Large Soil Monoliths. *Water Air Soil Poll.* **2003**, *143* (1/4), 3−21.

(14) Deb, D.; Chakma, S. Colloid and colloid-facilitated contaminant transport in subsurface ecosystem—a concise review. *International Journal of Environmental Science and Technology* **2023**, *20* (6), 6955−6988.

(15) Syngouna, V. I.; Chrysikopoulos, C. V. Cotransport of clay colloids and viruses in water saturated porous media. *Colloids Surf., A* **2013**, *416*, 56−65.

(16) Syngouna, V. I.; Chrysikopoulos, C. V. Experimental investigation of virus and clay particles cotransport in partially saturated columns packed with glass beads. *J. Colloid Interface Sci.* **2015**, *440*, 140−150.

(17) Syngouna, V. I.; Chrysikopoulos, C. V. Cotransport of clay colloids and viruses through water-saturated vertically oriented columns packed with glass beads: Gravity effects. *Science of The Total Environment* **2016**, *545−546*, 210−218.

(18) Chrysikopoulos, C. V.; Sotirelis, N. P.; Kallithrakas-Kontos, N. G. Cotransport of Graphene Oxide Nanoparticles and Kaolinite Colloids in Porous Media. *Transport in Porous Media* **2017**, *119* (1), 181−204.

(19) Wu, M.; Bi, E.; Li, B. Cotransport of nano-hydroxyapatite and different Cd(II) forms influenced by fulvic acid and montmorillonite colloids. *Water Res.* **2022**, *218*, No. 118511.

(20) Zhan, W.; Liu, G.; Hu, E.; Zhang, J.; Huo, L.; Zhong, H. Cotransport of fullerene nanoparticles and clay colloids in porous media: The relation between aggregation and transport. *Journal of Hazardous Materials* **2025**, *481*, No. 136535.

(21) Kleber, M.; Sollins, P.; Sutton, R. A conceptual model of organo-mineral interactions in soils: self-assembly of organic molecular fragments into zonal structures on mineral surfaces. *Biogeochemistry* **2007**, *85* (1), 9−24.

(22) Gao, J.; Mikutta, R.; Jansen, B.; Guggenberger, G.; Vogel, C.; Kalbitz, K. The multilayer model of soil mineral−organic interfaces—a review. *Journal of Plant Nutrition and Soil Science* **2020**, *183* (1), 27−41.

(23) Kwon, J.-H.; Ji, M.-K.; Kumar, R.; Islam, M. M.; Khan, M. A.; Park, Y.-K.; Yadav, K. K.; Vaziri, R.; Hwang, J.-H.; Lee, W. H.; Ahn, Y.-T.; Jeon, B.-H. Recent advancement in enhanced soil flushing for remediation of petroleum hydrocarbon-contaminated soil: a state-of-the-art review. *Reviews in Environmental Science and Bio/Technology* **2023**, *22* (3), 679−714.

(24) Ma, J.; Guo, H.; Lei, M.; Li, Y.; Weng, L.; Chen, Y.; Ma, Y.; Deng, Y.; Feng, X.; Xiu, W. Enhanced transport of ferrihydrite colloid by chain-shaped humic acid colloid in saturated porous media. *Science of The Total Environment* **2018**, *621*, 1581−1590.

(25) Chen, Y.; Ma, J.; Li, Y.; Weng, L. Enhanced cadmium immobilization in saturated media by gradual stabilization of goethite in the presence of humic acid with increasing pH. *Science of The Total Environment* **2019**, *648*, 358−366.

(26) Ma, J.; Qiu, Y.; Zhao, J.; Ouyang, X.; Zhao, Y.; Weng, L.; Md Yasir, A.; Chen, Y.; Li, Y. Effect of Agricultural Organic Inputs on Nanoplastics Transport in Saturated Goethite-Coated Porous Media: Particle Size Selectivity and Role of Dissolved Organic Matter. *Environ. Sci. Technol.* **2022**, *56* (6), 3524−3534.

(27) Hou, W.; Lei, Z.; Hu, E.; Wang, H.; Wang, Q.; Zhang, R.; Li, H. Cotransport of uranyl carbonate loaded on amorphous colloidal silica and strip-shaped humic acid in saturated porous media: Behavior and mechanism. *Environ. Pollut.* **2021**, *285*, No. 117230.

(28) Wang, M.; Lu, T.; Chen, W.; Zhang, H.; Qi, W.; Song, Y.; Qi, Z. Enhanced role of humic acid on the transport of iron oxide colloids in saturated porous media under various solution chemistry conditions. *Colloids Surf., A* **2020**, *607*, No. 125486.

(29) Tran, H. T.; Lin, C.; Bui, X. T.; Ngo, H. H.; Cheruiyot, N. K.; Hoang, H. G.; Vu, C. T. Aerobic composting remediation of petroleum hydrocarbon-contaminated soil. Current and future perspectives. *Science of The Total Environment* **2021**, *753*, No. 142250.

(30) Barros, E. V.; Filgueiras, P. R.; Lacerda, V.; Rodgers, R. P.; Romão, W. Characterization of naphthenic acids in crude oil samples−A literature review. *Fuel* **2022**, *319*, No. 123775.

(31) Shim, H.; Ma, W.; Lin, A.; Chan, K. Bio-removal of mixture of benzene, toluene, ethylbenzene, and xylenes/total petroleum hydrocarbons/trichloroethylene from contaminated water. *Journal of Environmental Sciences* **2009**, *21* (6), 758−763.

(32) Gebregiorgis Ambaye, T.; Vaccari, M.; Franzetti, A.; Prasad, S.; Formicola, F.; Rosatelli, A.; Hassani, A.; Aminabhavi, T. M.; Rtimi, S. Microbial electrochemical bioremediation of petroleum hydrocarbons (PHCs) pollution: Recent advances and outlook. *Chemical Engineering Journal* **2023**, *452*, No. 139372.

(33) Ghosh, P.; Mukherji, S. Degradation of carbazole, fluorene, dibenzothiophene and their mixture by *P. aeruginosa* RS1 in petroleum refinery wastewater. *Journal of Water Process Engineering* **2020**, *37*, No. 101454.

(34) Wu, J.; Ye, Q.; Wu, P.; Xu, S.; Liu, Y.; Ahmed, Z.; Rehman, S.; Zhu, N. Heteroaggregation of nanoplastics with oppositely charged minerals in aquatic environment: Experimental and theoretical calculation study. *Chemical Engineering Journal* **2022**, *428*, No. 131191.

(35) Lu, T.; Manzetti, S. Wavefunction and reactivity study of benzo[a]pyrene diol epoxide and its enantiomeric forms. *Structural Chemistry* **2014**, *25* (5), 1521−1533.

(36) Ma, J.; Li, J.; Weng, L.; Ouyang, X.; Chen, Y.; Li, Y. Phosphorus-Enhanced and Calcium-Retarded Transport of Ferrihydrite Colloid: Mechanism of Electrostatic Potential Changes Regulated via Adsorption Speciation. *Environ. Sci. Technol.* **2023**, *57* (10), 4219−4230.

(37) Zhang, M.; Bradford, S. A.; Klumpp, E.; Simunek, J.; Wang, S.; Wan, Q.; Jin, C.; Qiu, R. Significance of Non-DLVO Interactions on the Co-Transport of Functionalized Multiwalled Carbon Nanotubes and Soil Nanoparticles in Porous Media. *Environ. Sci. Technol.* **2022**, *56* (15), 10668−10680.

(38) Yasir, A. M.; Ma, J.; Ouyang, X.; Zhao, J.; Zhao, Y.; Weng, L.; Islam, M. S.; Chen, Y.; Li, Y. Effects of selected functional groups on nanoplastics transport in saturated media under diethylhexyl phthalate co-contamination conditions. *Chemosphere* **2022**, *286* (Pt 3), No. 131965.

(39) Saiers, J. E.; Hornberger, G. M. The role of colloidal kaolinite in the transport of cesium through laboratory sand columns. *Water Resour. Res.* **1996**, *32* (1), 33−41.

(40) Chrysikopoulos, C. V.; Syngouna, V. I. Effect of gravity on colloid transport through water-saturated columns packed with glass beads: modeling and experiments. *Environ. Sci. Technol.* **2014**, *48* (12), 6805−6813.

(41) Chen, K. L.; Elimelech, M. Aggregation and deposition kinetics of fullerene (C60) nanoparticles. *Langmuir* **2006**, *22* (26), 10994−11001.

(42) Qian, X.; Ma, J.; Weng, L.; Chen, Y.; Ren, Z.; Li, Y. Influence of agricultural organic inputs and their aging on the transport of ferrihydrite nanoparticles: From enhancement to inhibition. *Science of The Total Environment* **2020**, *719*, No. 137440.

(43) Bradford, S. A.; Simunek, J.; Bettahar, M.; van Genuchten, M. T.; Yates, S. R. Modeling colloid attachment, straining, and exclusion in saturated porous media. *Environ. Sci. Technol.* **2003**, *37* (10), 2242−2250.

(44) Yu, B.; Jia, S. Y.; Liu, Y.; Wu, S. H.; Han, X. Mobilization and re-adsorption of arsenate on ferrihydrite and hematite in the presence of oxalate. *Journal of Hazardous Materials* **2013**, *262*, 701−708.

(45) Verwey, E. J. W.; Overbeek, J. T. G. *Theory of the stability of lyophobic colloids*; Elsevier: Amsterdam, 1948.

(46) Derjaguin, B.; Landau, L. Theory of the stability of strongly charged lyophobic sols and of the adhension of strongly charged particles in solutions of electrolytes. *Acta Physicochim. U. R. S. S.* **1941**, *14*, 733−762.

(47) Lu, T. *Molclus program, Version 1.12*, http://www.keinsci.com/research/molclus.html. (accessed Aug 23, 2023).

(48) Lu, T.; Chen, F. Multiwfn: a multifunctional wavefunction analyzer. *J. Comput. Chem.* **2012**, *33* (5), 580−592.

(49) Kühne, T. D.; Iannuzzi, M.; Del Ben, M.; Rybkin, V. V.; Seewald, P.; Stein, F.; Laino, T.; Khaliullin, R. Z.; Schütt, O.; Schiffmann, F.; Golze, D.; Wilhelm, J.; Chulkov, S.; Bani-Hashemian, M. H.; Weber, V.; Borštnik, U.; Taillefumier, M.; Jakobovits, A. S.; Lazzaro, A.; Pabst, H.; Müller, T.; Schade, R.; Guidon, M.; Andermatt, S.; Holmberg, N.; Schenter, G. K.; Hehn, A.; Bussy, A.; Belleflamme, F.; Tabacchi, G.; Glöß, A.; Lass, M.; Bethune, I.; Mundy, C. J.; Plessl, C.; Watkins, M.; VandeVondele, J.; Krack, M.; Hutter, J. CP2K: An electronic structure and molecular dynamics software package - Quickstep: Efficient and accurate electronic structure calculations. *J. Chem. Phys.* **2020**, *152* (19), 194103.

(50) VandeVondele, J.; Krack, M.; Mohamed, F.; Parrinello, M.; Chassaing, T.; Hutter, J. Quickstep: Fast and accurate density functional calculations using a mixed Gaussian and plane waves approach. *Comput. Phys. Commun.* **2005**, *167* (2), 103−128.

(51) Klimes, J.; Bowler, D. R.; Michaelides, A. Chemical accuracy for the van der Waals density functional. *J. Phys.: Condens. Matter* **2010**, *22* (2), No. 022201.

(52) Van Der Spoel, D.; Lindahl, E.; Hess, B.; Groenhof, G.; Mark, A. E.; Berendsen, H. J. GROMACS: fast, flexible, and free. *J. Comput. Chem.* **2005**, *26* (16), 1701−1718.

(53) Abraham, M. J.; Murtola, T.; Schulz, R.; Páll, S.; Smith, J. C.; Hess, B.; Lindahl, E. GROMACS: High performance molecular simulations through multi-level parallelism from laptops to supercomputers. *SoftwareX* **2015**, *1−2*, 19−25.

(54) Berendsen, H. J. C.; van der Spoel, D.; van Drunen, R. GROMACS: A message-passing parallel molecular dynamics implementation. *Comput. Phys. Commun.* **1995**, *91* (1−3), 43−56.

(55) Rappe, A. K.; Casewit, C. J.; Colwell, K. S.; Goddard, W. A.; Skiff, W. M. UFF, a full periodic table force field for molecular mechanics and molecular dynamics simulations. *J. Am. Chem. Soc.* **1992**, *114* (25), 10024−10035.

(56) Jorgensen, W. L.; Maxwell, D. S.; Tirado-Rives, J. Development and Testing of the OPLS All-Atom Force Field on Conformational Energetics and Properties of Organic Liquids. *J. Am. Chem. Soc.* **1996**, *118* (45), 11225−11236.

(57) Chen, H.; Hou, M.; He, Z.; Liang, Y.; Xu, J.; Tan, W. Adsorption behavior of soil fulvic acid on crystal faces of kaolinite and goethite: Described by CD-MUSIC model. *Science of The Total Environment* **2023**, *903*, No. 165806.

(58) Weng, L.; Van Riemsdijk, W. H.; Koopal, L. K.; Hiemstra, T. Ligand and Charge Distribution (LCD) model for the description of fulvic acid adsorption to goethite. *J. Colloid Interface Sci.* **2006**, *302* (2), 442−457.

(59) Madejová, J.; Komadel, P. Baseline Studies of the Clay Minerals Society Source Clays: Infrared Methods. *Clays and Clay Minerals* **2001**, *49* (5), 410−432.

(60) Zhao, H.; Gu, B.; Chen, D.; Tang, J.; Xu, X.; Qiao, Z.; Wang, J. Physicochemical properties and salinization characteristics of soils in coastal land reclamation areas: A case study of China-Singapore Tianjin Eco-City. *Heliyon* **2022**, *8* (12), No. e12629.

(61) Liu, Y.; Ma, J.; Feng, B.; Zhang, X.; Zhao, Y.; Weng, L.; Chen, Y.; Xie, H.; Li, Y. Effect of isomeric polysaccharides on heteroaggregation of nanoplastics in high ionic strength conditions: Synergies of morphology and molecular conformation. *Journal of Hazardous Materials* **2024**, *480*, No. 135818.

(62) Al-Bazali, T. A critical investigation of diffuse double layer changes in clay-electrolyte systems at high temperatures. *Journal of Geophysics and Engineering* **2022**, *19* (4), 940−954.

(63) Zong, D.; Xu, H.; Ding, M.; Yao, C.; Lin, T.; Gao, L. Effect of the cations on the humic acid induced membrane fouling in the membrane distillation process. *Desalination* **2024**, *577*, No. 117398.

(64) Chrysikopoulos, C. V.; Katzourakis, V. E. Colloid particle size-dependent dispersivity. *Water Resour. Res.* **2015**, *51* (6), 4668−4683.

(65) Liao, P.; Li, W.; Wang, D.; Jiang, Y.; Pan, C.; Fortner, J. D.; Yuan, S. Effect of reduced humic acid on the transport of ferrihydrite nanoparticles under anoxic conditions. *Water Res.* **2017**, *109*, 347−357.

(66) Wang, D.; Zhang, W.; Zhou, D. Antagonistic effects of humic acid and iron oxyhydroxide grain-coating on biochar nanoparticle

transport in saturated sand. *Environ. Sci. Technol.* **2013**, *47* (10), 5154−5161.

(67) Wu, Z.; Wu, S.; Hou, Y.; Cao, H.; Cai, C. Facilitated transport of toluene and naphthalene with humic acid in high- and low-permeability systems: Role of ionic strength and cationic type. *Journal of Hazardous Materials* **2024**, *465*, No. 133487.

(68) Lefebvre, C.; Rubez, G.; Khartabil, H.; Boisson, J. C.; Contreras-Garcia, J.; Henon, E. Accurately extracting the signature of intermolecular interactions present in the NCI plot of the reduced density gradient versus electron density. *Phys. Chem. Chem. Phys.* **2017**, *19* (27), 17928−17936.

(69) Zadeh, S. S.; Ebrahimi, A.; Shahraki, A. The impact of pi-pi stacking interactions on photo-physical properties of hydroxyanthraquinones. *Spectrochimica Acta - Part A: Molecular and Biomolecular* **2023**, *292*, No. 122453.

(70) Hiemstra, T.; Van Riemsdijk, W. H. On the relationship between charge distribution, surface hydration, and the structure of the interface of metal hydroxides. *J. Colloid Interface Sci.* **2006**, *301* (1), 1−18.

(71) Marín-García, D. C.; Adams, R. H.; Hernández-Barajas, R. Effect of crude petroleum on water repellency in a clayey alluvial soil. *International Journal of Environmental Science and Technology* **2016**, *13* (1), 55−64.

(72) Weng, L.; Van Riemsdijk, W. H.; Hiemstra, T. Humic Nanoparticles at the Oxide−Water Interface: Interactions with Phosphate Ion Adsorption. *Environ. Sci. Technol.* **2008**, *42* (23), 8747−8752.

(73) Wilkes, H.; Schwarzbauer, J. Hydrocarbons: An Introduction to Structure, Physico-Chemical Properties and Natural Occurrence. In *Handbook of Hydrocarbon and Lipid Microbiology*, Timmis, K. N. Ed.; Springer, 2010.

(74) Li, X.; Li, Y.; Wang, H.; Qin, S.; Wang, X.; Yang, H.; Cornelis, W. Ecological restoration evaluation of afforestation in Gudao Oilfield based on multi-source remote sensing data. *Ecological Engineering* **2023**, *197*, No. 107107.

(75) Zhang, X.; Qi, A.; Wang, P.; Huang, Q.; Zhao, T.; Yang, L.; Wang, W. Influence of oil extraction on concentration distributions, migration, secondary formation and carcinogenic risk of NPAHs and OPAHs in air and soil in an oilfield development area in China. *Science of The Total Environment* **2024**, *922*, No. 170736.

(76) Zhao, X.; Pu, X.; Jiang, W.; Zhou, L.; Jin, F.; Xiao, D.; Fu, L.; Li, H. An exploration breakthrough in Paleozoic petroleum system of Huanghua Depression in Dagang Oilfield and its significance North China. *Petroleum Exploration and Development* **2019**, *46* (4), 651−663.

(77) Chen, X.; Xu, S.; Li, S.; He, H.; Han, Y.; Qu, X. Identification of architectural elements based on SVM with PCA: A case study of sandy braided river reservoir in the Lamadian Oilfield, Songliao Basin, NE China. *J. Pet. Sci. Eng.* **2021**, *198*, No. 108247.

(78) Katzourakis, V. E.; Chrysikopoulos, C. V. Mathematical modeling of colloid and virus cotransport in porous media: Application to experimental data. *Advances in Water Resources* **2014**, *68*, 62−73.

(79) Katzourakis, V. E.; Chrysikopoulos, C. V. Modeling dense-colloid and virus cotransport in three-dimensional porous media. *Journal of Contaminant Hydrology* **2015**, *181*, 102−113.